

**Phonon Softening Induced Phase Transition of CeSiO₄: A
Density Functional Theory Study**

Journal:	<i>Dalton Transactions</i>
Manuscript ID	DT-ART-01-2024-000179.R1
Article Type:	Paper
Date Submitted by the Author:	23-Feb-2024
Complete List of Authors:	Zhao, Xiaodong; Washington State University College of Arts and Sciences, Chemistry Strzelecki, Andrew; Washington State University College of Arts and Sciences, Chemistry Dacheux, Nicolas; University of Montpellier, ICSM, CEA, CNRS, ENSCM, Univ Montpellier Qi, Liang; University of Michigan, Department of Materials Science and Engineering Guo, Xiaofeng; Washington State University College of Arts and Sciences, Chemistry; Los Alamos National Laboratory, EES

Phonon Softening Induced Phase Transition of CeSiO₄: A Density Functional Theory Study

Xiaodong Zhao,¹ Andrew C. Strzelecki,^{2,3} Nicolas Dacheux⁴, Liang Qi,^{5*} Xiaofeng Guo^{1,2*}

1. Department of Chemistry, Washington State University, Pullman, Washington, 99164, United States
2. School of Mechanical and Materials Engineering, Washington State University, Pullman, Washington, 99164, United States
3. Earth and Environmental Sciences Division, Los Alamos National Laboratory, Los Alamos, New Mexico, 87545, United States
4. ICSM, Univ Montpellier, CNRS, CEA, ENSCM, Site de Marcoule, Bagnols sur Cèze, 30207, France
5. Department of Materials Science and Engineering, University of Michigan, Ann Arbor, Michigan, 48109, United States

Abstract:

Density functional theory plus Hubbard U (DFT+ U) methodology was used to calculate the structures and energetic landscapes of CeSiO₄, including its stetindite and scheelite phases from ambient pressure to ~ 24 GPa. To ensure accurate simulations of the high-pressure structures, assessments of strain-stress methods and stress-strain methods were conducted in prior, with the former found to have a better agreement with the experimental result. From DFT calculations the equation of states (EOS) of both stetindite and scheelite were further obtained, with the fitted bulk moduli being 182(2) GPa and 190.0(12) GPa, respectively. These results were found to be consistent with the experimental values of 177(5) GPa and 222(40) GPa. Furthermore, the calculated energetics suggest that the stetindite structure is more thermodynamically stable than the scheelite structure at a pressure lower than 8.35 GPa. However, the stetindite \rightarrow scheelite phase transition was observed experimentally at a much higher pressure of ~ 15 GPa. A further phonon spectra investigation by the density functional perturbation theory (DFPT) indicated the E_g^1 mode is being softened with pressure and becomes imaginary after 12 GPa, which is a sign of the lattice instability. Consequently, it was concluded that the stetindite \rightarrow scheelite transition is predominantly initiated by the lattice instability under high-pressure.

Keywords: Zircon, Stetindite, Phase Transition, Softened Phonon, Lattice Dynamics, High-Pressure, Thermodynamics

Introduction

Minor actinides in the radioactive waste, including neptunium (Np), plutonium (Pu), americium (Am) and curium (Cm), pose substantial challenges in terms of their long-term management and secure disposal due to their long half-life, high radiotoxicity and biotoxicity.¹⁻³ In the United States, there are two primary resources of actinide radioactive waste: (i) the spent nuclear fuel (SNF) from nuclear power plants (NPPs). Typical nuclear power plant (NPP) generating ~ 1 GW-e per year produces ~ 25 tonnes of SNF are produced by NPP generating ~ 1 GW-e per year.⁴ The US is following a 'once-through' processing policy, which means the residue uranium (U), Pu and other minor actinides are not reprocessed and retrieved from the SNF, all these actinides will be solidified and directly disposed in the future deep geological site. In countries with reprocessing and nuclear fuel cycle policies, like France, the PUREX process is utilized, in which process the U and Pu is extracted, and minor actinides from the 1st cycle 1AW raffinate is vitrified and will be disposed in deep geological site;⁵ (ii) the significant accumulation of plutonium by the US nuclear weapon program from World War II to cold war.⁶ The weapon grade plutonium does not only raise environmental issues but also non-proliferation concerns.⁷⁻⁹ It is crucial to safely dispose the radioactive waste and isolate them out of any biospheres. Various forms, including glasses, ceramics, and glass-ceramics forms have been proposed to enclose the spent nuclear fuel or high-level waste (HLW).^{10, 11} Among them, ceramic form has been highly recommended for actinide immobilization, especially the fluorite-related structure (cubic zirconia, pyrochlore, zircon, murataite etc.).⁴ Actinide orthosilicates (AnSiO_4 , where An = Th-Am),^{12, 13} possessing the zircon structure (space group $I4_1/amd$, as in Fig. 1), have emerged as a promising candidate matrix for immobilizing minor actinides due to its remarkable attributes, such as minimal chemical reactivity, low solubility, and robust resistance to radiation-induced damage.^{2, 14-17} Additionally, aside from its role as a nuclear waste disposal matrix, zircon-structured phase is also being considered as an alteration form during the long-term nuclear waste storage.¹⁸ Most actinide nuclei and the decay daughter nuclei have long half-lives, such as $T_{1/2, \text{Pu-241}} = 14.4$ years and its second daughter nuclei $T_{1/2, \text{Np-237}} = 2.1$ million years.¹⁹ In such a long timescale, minor actinides in the deep geological site may get leached from the host matrix and contact with the silica in the back-filled clay and geological barrier of granite, hence could trigger the formation of zircon. It is also evidenced that zircon-structured phases have been found in the nuclear accident sites,^{1, 20-23} from the high temperature-pressure reaction of actinides with the natural abundant silica-minerals (e.g. quartz). To ensure the secure nuclear waste disposal over extended periods, it is essential to understand its stability, structural behavior, and transformation mechanisms under extreme conditions.²⁴

More recently, DFT calculation revealed that the phase transformation mechanism of coffinite (USiO_4) is governed by both the thermodynamic and lattice instability factors: enthalpy of the scheelite-type USiO_4 becomes lower than the coffinite phase at around 16 GPa²⁵ and the B_{2u} silent mode becomes imaginary at around 12.5 GPa²⁶ aligning well with the experimental phase transition pressure observed at around 15 GPa.²⁵ However, there is less research on CeSiO_4 stetindite, especially on the theoretical side^{27, 28}, with only one study present in the literature.²⁹ To date, there is only one experimental study of CeSiO_4 under high pressures.³⁰ In practice, stetindite (CeSiO_4) can be served as a suitable analogue^{17, 31} to PuSiO_4 due to the inherent challenges

associated with handling plutonium and synthetic challenges to acquire pure phase of PuSiO_4 , a radioelement with high specific activity, as cerium carries both +3 and +4 charges and exhibits similar ionic radii to plutonium, allows for more manageable experimentation.³²⁻³⁵ *In situ* high-pressure Raman spectroscopy experiments and synchrotron X-ray diffraction have revealed that phase transition of stetindite differs from coffinite. Stetindite undergoes a phase transition to a newly characterized high-pressure low-symmetry (HPLS) polymorph (space group: $I\bar{4}_2d$) at approximately 15 GPa.³⁰ This transition results from slight rotational and torsional adjustments in the SiO_4 and MO_8 polyhedral within the zircon structure.³⁶ Further compression to 18 GPa leads to a transition to a scheelite structure type (space group: $I4_1/a$, as in Fig. 1).³⁰ However, a fundamental question remains unanswered: is the phase transition governed by enthalpy or lattice instabilities or both of them?

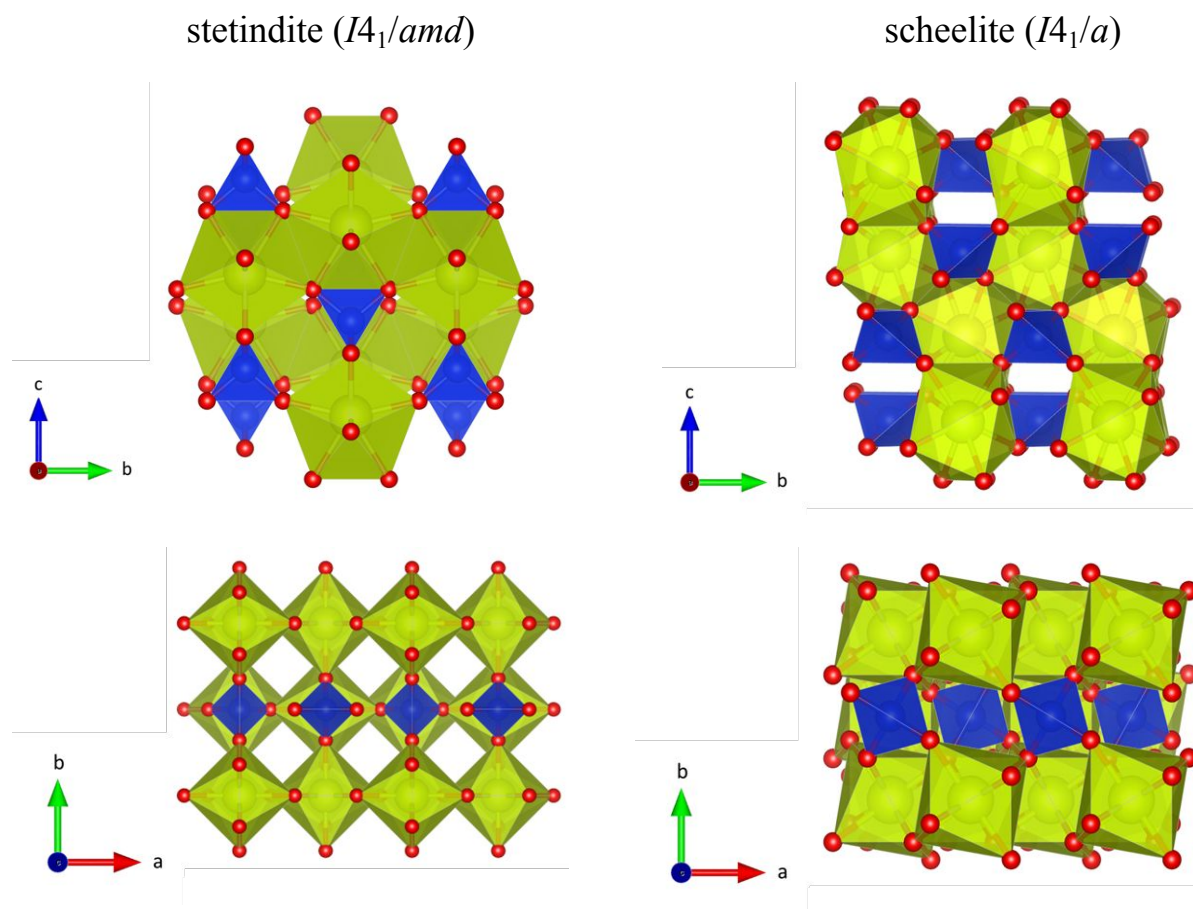


Figure 1 Crystal structures of the stetindite phase ($I4_1/amd$), and the high-pressure scheelite phase ($I4_1/a$). The yellow polyhedral is the octahedron from Ce-O and the blue polyhedral is the tetrahedron from Si-O. In the stetindite phase, the Ce-O octahedron is sharing edge with the Si-O tetrahedron, while in the scheelite phase, the Ce-O octahedron is sharing corner with the Si-O tetrahedron.

This paper extends the scope of lattice dynamics studies and provides a comprehensive analysis of the phonon spectra phases, with a specific focus on the properties of the soft mode. Employing first-principles calculations, the structural and dynamic properties during the phase transition from

stetindite to scheelite were delved into. Pressure is applied using a strain-stress method, and phonon-dispersion curves are obtained through density functional perturbation theory (DFPT) methodology. The calculation methods will be presented in the Methodology section. The external pressure simulation and crystal structural evolution under varying pressures, with their corresponding phonon dispersion curves will be discussed in the Results and Discussion section.

II. Methodology

Periodic DFT+ U calculations were performed by using Vienna Ab initio Simulation Package (VASP) 5.4.4.³⁷⁻⁴⁰ Generalized gradient approximation (GGA) approximation was used for the exchange-correlation function, and projector-augment wave (PAW) pseudopotentials were used for the core electrons.^{41, 42} GW-PAW potentials was selected based on initial testing with various pseudopotentials. This pseudopotential with GW approximation, introduced by VASP, can be applicable in both DFT and GW calculations to deliver highly accurate results. The selection of GW-PAW potentials demonstrated a volume discrepancy of merely 2% to 2.5% compared with experimental data, which is well within the acceptable error range for DFT calculations in the VASP framework. The valence electrons of cerium, silicon, and oxygen were respectively set as $5s^25p^64f^15d^16s^2$, $2s^22p^63s^23p^2$, and $2s^22p^4$. The 2s electrons of silicon were also regarded as valence electrons. Cutoff energy was set to be 700 eV, and this high energy cutoff value is more computationally expensive, but it ensured the accuracy to represent the role of electrons under high-pressure. The strong on-site repulsion force of highly localized cesium 4f electrons necessarily needs to be considered in the compacted high-P structure, hence an effective Hubbard U of 4.0 eV was set for 4f electron.⁴³ In ionic and electronic optimization steps, total energy was converged to 1×10^{-5} eV and force between ions was converged to 1×10^{-4} eV \AA^{-1} . Sampling mesh in Brillion zone was set to be $7 \times 7 \times 7$ based on convergence study. All the calculations were performed at nearly 0 K, and the acquired lattice constants and enthalpy maybe different with measured results in experiments. The thermal expansion at high temperate, and anharmonic vibrational behavior could all make the measured lattice constant differ from DFT+ U results. The approximation in the treatment of electron-electron interaction (e.g. exchange-correlation functional) and neglection of zero-point vibrations at 0 K will also make the computed enthalpy values be a bit different with the real case. In this work, DFT results are always compared with available experimental results, and also make complement to the experiments by providing insights which is hard to be measured, such as the thermodynamic properties at high-pressure.

The density functional perturbation theory (DFPT) in the harmonic approximation in the PHONOPY package was applied to compute the phonon modes.⁴⁴⁻⁴⁷ DFPT is a methodology that builds upon DFT, which perturbs the atomic positions from their equilibrium positions along symmetry-unique directions.⁴⁴ The energy and restoring force are calculated employing VASP and are used for subsequent processing in PHONOPY for calculations of corresponding force constants. A $2 \times 1 \times 1$ supercell was used throughout the calculations to avoid unphysical self-interaction of the perturbed atoms due to the periodic conditions. Only the vibrations at the Γ -point of the Brillouin (i.e., $q = 0$) was considered for the assignment of irreducible representations to each mode at the center of the Brillouin zone according to the character table of the underlying point group which

the structure belongs to, i.e. D_{4h} ($4/mmm$) for zircon.⁴⁸ And the eigenmodes were assigned by the comparison based on previous research of $ZrSiO_4$ and $USiO_4$ at ambient condition.^{25, 26, 49, 50}

To apply an external hydrostatic force to the system, two computational techniques can be used. The first method is the strain-stress approach, where lattice parameters are adjusted, and the induced Hellmann–Feynman force serves as the hydrostatic force.^{51, 52} To create a uniaxial hydrostatic pressure by strain-stress method, the strain tensor needs to be diagonal. A new unit cell is built upon a hydrostatic pressure as equation (1):

$$A' = A \cdot \varepsilon_{ij} = \begin{bmatrix} a & 0 & 0 \\ 0 & a & 0 \\ 0 & 0 & c \end{bmatrix} \begin{bmatrix} 1 - \delta & 0 & 0 \\ 0 & 1 - \delta & 0 \\ 0 & 0 & 1 - \delta' \end{bmatrix} = \begin{bmatrix} (1 - \delta) \cdot a & 0 & 0 \\ 0 & (1 - \delta) \cdot a & 0 \\ 0 & 0 & (1 - \delta') \cdot c \end{bmatrix} \#(1)$$

Where A' and A matrix contain the cell lattice vectors in Cartesian form, ε_{ij} is the diagonal strain tensor.⁵³

Besides the diagonal components, all the other values in the strain tensor are kept as zero to eliminate the shear stress. The stress force is calculated by the first derivatives of energy with respect to the strain by equation (2),

$$\sigma_{ij} = \frac{1}{V} \frac{\partial E}{\partial \varepsilon_{ij}} \#(2)$$

Where E is energy, and the σ_{ij} is the stress tensor.

In VASP 5.4.4, the stress tensor is computed following the Hellman-Feynman theorem^{52, 54} and can be directly read from the output files by the convention of σ_i , where i runs from 1-6 following the notation of xx, yy, zz, yz, xz, xy.⁵⁵ Hence, in VASP 5.4.4, the stress tensor can be expressed as equation (3):

$$\begin{bmatrix} \sigma_{11} & \sigma_{12} & \sigma_{13} \\ \sigma_{12} & \sigma_{22} & \sigma_{23} \\ \sigma_{13} & \sigma_{23} & \sigma_{33} \end{bmatrix} = \begin{bmatrix} \sigma_1 & \sigma_6 & \sigma_5 \\ \sigma_6 & \sigma_2 & \sigma_4 \\ \sigma_5 & \sigma_4 & \sigma_3 \end{bmatrix} = \begin{bmatrix} \sigma_{xx} & \sigma_{xy} & \sigma_{xz} \\ \sigma_{xy} & \sigma_{yy} & \sigma_{yz} \\ \sigma_{xz} & \sigma_{yz} & \sigma_{zz} \end{bmatrix} \#(3)$$

In all the calculations, by adjusting the external strain δ and δ' in equation (1), only the diagonal components of the stress tensor σ_{xx} , σ_{yy} and σ_{zz} are kept-non-zero, and the difference of each stress is within 1%. The final hydrostatic pressure scalar is obtained as the trace of the matrix divided by three, as shown in equation (4):

$$\sigma_i = -P \varepsilon_i \#(4)$$

Hence the calculation of the diagonal stress tensor makes the pressure P and the enthalpy $H = E + PV$ accessible.⁵⁶ The unit cell was systematically compressed and expanded, with identical structures from both methods and further confirmed by the material's consistent return to equilibrium positions after random atomic perturbations (Fig. S1).

The second method is the stress-strain approach, which employs Pulay stress to affect the system, permitting volume relaxation. To ensure the accuracy of the Pulay stress-relaxed structure, a secondary relaxation of the lattice was carried out, followed by energy calculations using the tetrahedron method (the whole flow-chart is shown in Fig. S2).⁵⁴

III. Results and Discussion

3.1 High-Pressure Structures and Enthalpies

A comparison of these two methodologies was conducted to assess the precision of both the strain-stress and stress-strain methods and is shown in Fig. S3. It is shown that the strain-stress method better approximates the experimental volumes under high-pressure, despite minor disparities between the two methods. The simulation also extends the stetindite structure beyond the phase transition at approximately 10 GPa, after which pressure the stetindite phase is not trackable by experiments. This enables us to investigate the underlying mechanism of stetindite instability beyond 10 GPa. Nevertheless, a noticeable discrepancy emerges in the energy calculation of about 70 kJ/mol. Considering the strain-stress method is more accurate in the structural aspect, the enthalpy values derived from strain-stress method was chosen for further analysis. Enthalpy values are determined as $H = U + PV$, and the results from both methods exhibit substantial similarity. Internal energy values encompass energies from the eigenvalues of the static Schrodinger equation, incorporating potential energy components such as electrostatic (alpha Z and Ewald energy), Hartree, and exchange-correlation energies.⁵⁷ The external work is calculated as $P \times V$, with P derived from the generated Hellmann-Feynman force or set Pulay stress.

After the tests, the strain-stress method was selected due to its high accuracy. The computed unit cell parameters and enthalpy values for stetindite and scheelite are summarized in Tables 1 and 2, respectively. The pressure dependence of computed unit cell volumes for two CeSiO_4 phases, in comparison with experimental values, were shown in Fig. S3. Both the experimental and simulated values were fitted using the second-order Birch–Murnaghan equation of state (BMEOS), as shown in the equation (5) below:⁵⁸

$$P = \frac{3K_0}{2} \left[\left(\frac{V_0}{V} \right)^{\frac{7}{3}} - \left(\frac{V_0}{V} \right)^{\frac{5}{3}} \right] \#(5)$$

Here V_0 represents the zero-pressure unit cell volume, V is the cell volume at a given pressure (P), and K_0 denotes the bulk modulus. The fits were carried out using the EosFit7 software, which offers the option to incorporate the uncertainties of the data points in the fitting process.⁵⁹

The DFT calculations for stetindite produced EOS closely matching the experimental values, as the calculated zero-pressure unit cell volume and bulk modulus for stetindite are 306.1(2) \AA^3 and 182(2) GPa, respectively, consistent with the experimental values of 300.4(2) \AA^3 and 177(5) GPa. The fitted curve also displayed similar convergence, affirming the agreement. Conversely, the calculations for scheelite yielded a zero-pressure unit cell volume of 277.5(10) \AA^3 and a bulk

modulus of 190.0(12) GPa. The EOS fitting for the calculated values differ slightly from the experimental ones, which are 276(3) A³ and 222(40) GPa. The bulk modulus from the experimental results fitting is larger than the fitted result from the calculations, also carrying a larger error, which could be due to the scattered nature of the experimental data at high-pressure ranges. These can be seen from the divergence between the fitted curves for scheelite based on the calculated and experimental results.

Table 1 Unit cell parameters and enthalpy values of stetindite under high pressures up to ~24 GPa.

simulated pressure / GPa	a / Å	c / Å	volume / Å ³	enthalpy / kJ·mol ⁻¹
-0.23	7.06	6.27	312.52	-4750.34
4.11	6.98	6.24	304.19	-4548.21
8.37	6.92	6.21	297.30	-4354.78
12.45	6.87	6.18	291.39	-4173.61
16.05	6.82	6.16	286.76	-4016.59
19.88	6.78	6.13	282.21	-3852.28
23.98	6.74	6.11	277.74	-3678.80

Table 2 Unit cell parameters and enthalpy values of scheelite under high pressures up to ~24 GPa.

simulated pressure / GPa	a / Å	c / Å	volume / Å ³	enthalpy / kJ·mol ⁻¹
0.09	4.95	11.22	274.61	-4696.45
3.57	4.92	11.12	269.49	-4551.13
7.55	4.90	11.02	264.40	-4388.18
12.44	4.86	10.95	258.91	-4191.90
15.87	4.84	10.88	255.33	-4056.79
20.08	4.82	10.82	251.27	-3893.52
23.94	4.80	10.75	247.80	-3746.39

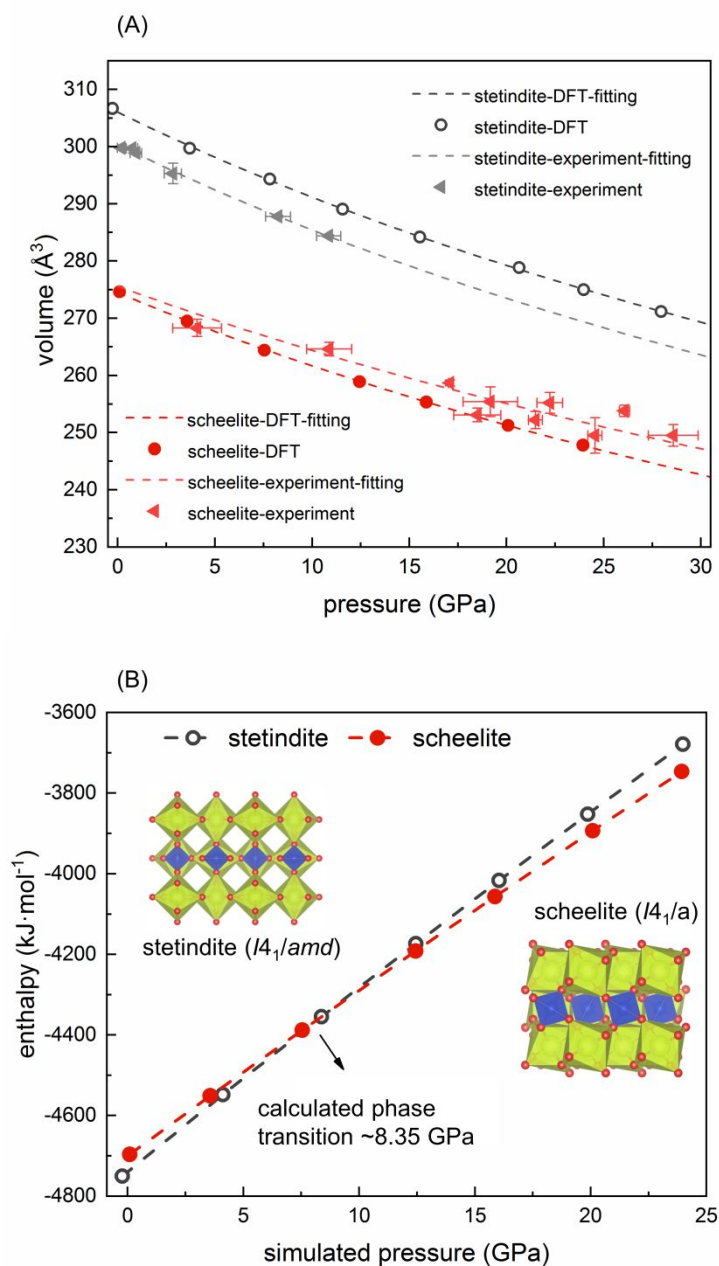
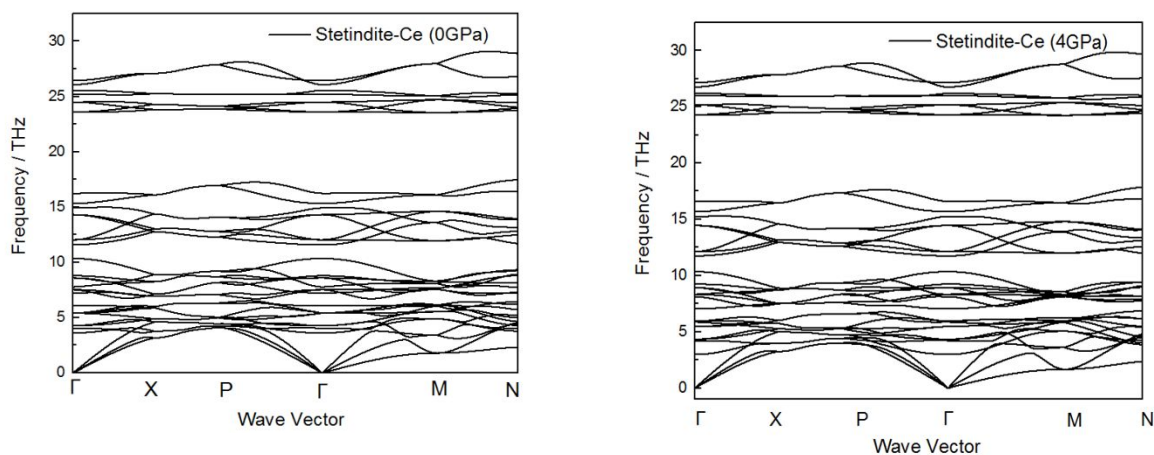


Figure 2 (A) Pressure-volume relationships of CeSiO_4 stetindite and scheelite CeSiO_4 . The dashed lines are fitting results by the second-order Birch-Murnaghan EOS fitting. Gray or red circle symbols are the results from DFT calculations, and gray or red triangle symbols are experimental values from synchrotron Rietveld refinement of synchrotron XRD.³⁰ The experimental data owns some statistical tolerance from the refinements, and the DFT approach is a deterministic approach, hence has no statistical errors. **(B)** Enthalpic landscape of stetindite and scheelite CeSiO_4 .

The calculated enthalpy results are presented in Fig. 2(B). The difference in enthalpy suggests that scheelite is the energetically more favorable phase under high pressure, with the phase transition

pressure around 8.35 GPa (lower than the experimental value³⁰). Even scheelite is more thermodynamic stable above 8.35 GPa, but this phase was not observed during the experiment. It is therefore hypothesized that there are two possible reasons for the difference in transitional pressure: (i) The activation energy barrier of the transition is higher than the enthalpy difference between stetindite and scheelite, and thus it requires higher pressure to surpass, (ii) The stetindite phase above 8.35 GPa could be thermodynamically metastable but kinetically stable, so the stetindite structure can be retained to a certain extent in pressure during experiment. Thirty random perturbation tests were conducted to test the hypothesis. The atoms are randomly perturbed by $-0.1 - 0.1 \text{ \AA}$ from its equilibrium position under 8 GPa, and it was found the atoms relaxed back to the original position all the time. The perturbation result indicated the stetindite structure may be dynamically stable, otherwise the atoms could not remain in place. On the other hand, this random perturbation was also intended to initially test if the phase transition could be a first-order phase transition, which process stochastically displaced atoms and the redistribution of atoms. However, by thirty random displacements, the structure maintained, which is consistent with the observation of an HPLS phase in the experiment that indicates a second-order phase transition or a diffusional transformation. Overall, the enthalpy cross-check point between stetindite and scheelite occurs at around 8.35 GPa, indicating that the scheelite phase is thermodynamically more stable than the stetindite phase beyond this pressure. However, the absence of a phase transition at this pressure suggests that it is not enthalpically driven and may involve lattice dynamics. Further evaluation of the phonon spectrum was conducted to gain a better understanding of the lattice dynamics.

3.2 High-Pressure Phonon Spectra



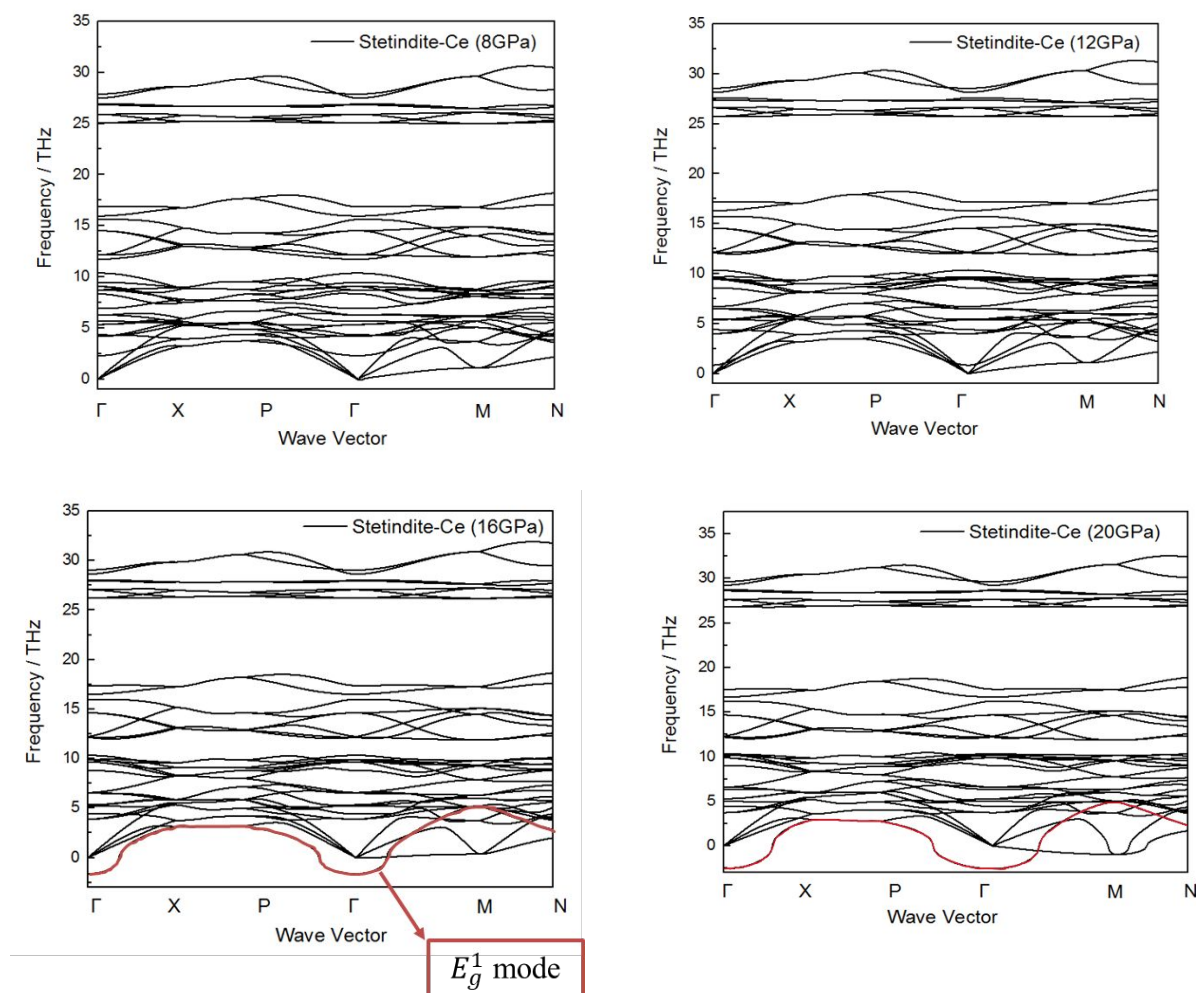


Figure 3 Phonon dispersion spectra of stetindite CeSiO_4 under different pressures.

The phonon spectra are displayed in Fig. 3, which arise from the 12 atoms within the primitive cell and give rise to a total of 36 vibration modes, encompassing 3 acoustic modes and 33 optical modes. The normal modes for stetindite (belonging to space group $I4_1/amd$, point group D_{4h}) can be represented as follows:

$$\Gamma_{acoustic} = E_u + A_{2u} \# \quad (5)$$

$$\Gamma_{optic} = 2A_{1g} + A_{2g} + A_{1u} + 3A_{2u} + 4B_{1g} + B_{2g} + B_{1u} + 2B_{2u} + 4E_u + 5E_g \# \quad (6)$$

The frequency-wavenumber dispersion curves were calculated through the high symmetry path $\Gamma - X - P - \Gamma - M - N$, which are respectively representing the points of Γ (0, 0, 0), X (0, 0, 1/2), P (1/4, 1/4, 1/4), M (-1/2, 1/2, 1/2) and N (0, 1/2, 0).⁵⁰ There are roughly two ranges in the curves, which are corresponding to the Ce-O motions (0 to ~17.5 THz) and Si-O motions (25 THz to 32 THz). The lowest three ones are the three lattice waves. This energy range agreed with previous calculations with zircon ZrSiO_4 , thorite ThSiO_4 and coffinite USiO_4 .^{26, 49, 58, 60-62} Given the iso-

structural fact between coffinite and stetindite, as well as the analogous trends observed in their phonon dispersion curves, the eigenmodes in stetindite were identified through a comparison with previous DFT calculations on coffinite. Specifically, modes with similar energetic order and dispersion curve shapes were identified as the same modes. However, it is worth mentioning the discrepancies in previous computational and experimental studies regarding the assignment of motional eigenmodes. For zircon ZrSiO_4 , two different orders have been reported: $E_g^1 < B_{1g}^1 < E_g^2 < E_g^3 < B_{1g}^2$ and $E_g^1 < B_{1g}^1 < E_g^2 < A_{2g} < B_{2g}$ (Raman spectrum of synthetic zircon (ZrSiO_4) and thorite (ThSiO_4)).^{49, 60} For coffinite, Li Su et. al. indicated the energetic order $E_g^1 < B_{1g}^1 < E_g^2 < E_g^3 < B_{1g}^2$,⁵⁰ however, J. D. Bauer et. al. showed different energetic order, $E_g^1 < B_{2g} < B_{1g}^1$.²⁶ The eigenvalues of the zircon modes exhibit notable distinctions compared to those of coffinite. For instance, the E_g^1 mode of zircon is twice that of coffinite. This divergence can be attributed to the substantial variation in reduced mean mass between U-O and Zr-O, as well as differences in bond strength. More research on the Raman modes identification is highly recommended in the future.

The dominant mode along the compression mode is the Raman active E_g^1 rotational mode. the E_g^1 mode's softening within the stetindite structure is a critical aspect of the high-pressure phase transition. This mode's frequency changes can be indicative of structural instability. At ambient condition, the E_g^1 mode shows a frequency of 3.62 THz, with increasing pressure, the mode E_g^1 shows a softening process. Between 12 and 16 GPa, E_g^1 mode was calculated as negative values, which is a sign of the instability of the stetindite phase. In this pressure range, the stetindite structure becomes unstable, leading to significant changes in the atomic arrangements to a low symmetry mode. Based on previous synchrotron XRD refinement, there is a HPLS phase (space group $I\bar{4}_2d$) between the transition of stetindite and scheelite phase.³⁰ There is no significant difference between the volume of stetindite phase ($V = 278.84(38) \text{ \AA}^3$ at $\sim 14.49 \text{ GPa}$) and the volume of HPLS phase ($V = 275.71(5) \text{ \AA}^3$ at $\sim 15.09 \text{ GPa}$).³⁰ The enthalpies of the two phases became close beyond 8.35 GPa and the volume showed continuity with the intermediate HPLS phase, suggesting a gradual rather than a discontinuous transition. Combining the experimental observation and the calculations in this work, a softening-mode driven second-order phase transition could be concluded. The twist of the oxygen cage results in the loss of the symmetry element of the reflection mirror normal to the x axis and the axial glide plane type of d to $[110]$ (as in Fig. 4), which explains the phase transformation from stetindite $I4_1/amd$ to scheelite $I4_1/a$. The E_g^1 mode has not been observed in the experiment due to the low frequency, and further low frequency Raman scattering experiment is highly recommended to scope the revolution of the E_g^1 mode. To gain a comprehensive understanding of this intriguing phase transition, further experiments, particularly low-frequency Raman scattering studies, are strongly recommended.

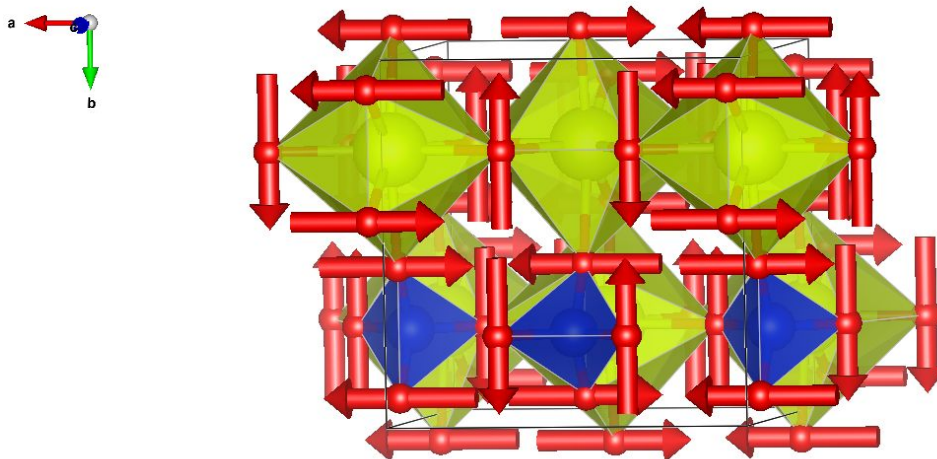


Figure 4 Preferable motion direction representation of the E_g^1 mode.

Overall, the DFT calculation revealed that the softening of the E_g^1 mode is the main driving force of the phase transition instead of enthalpy driving force, and a low symmetry intermediate phase is likely going to take place by the motion of the oxygens. In the future, the oxygen atoms will be perturbed according to the eigen vectors of the E_g^1 mode, and more investigation will be done to reveal the properties of the high-pressure low-symmetry phase.

IV. Conclusion

This study used a DFT+ U and DFPT methodology to investigate the phase transition mechanism of CeSiO₄ stetindite and scheelite under high-pressure. The calculated lattice parameters and bulk moduli by strain-stress method closely matched experimental values, confirming the reliability of the DFT calculations. Notably, it was observed that the enthalpy of stetindite remains lower than that of scheelite until pressures of approximately 8.35 GPa. Despite the scheelite phase being more thermodynamically stable than stetindite, at around 8.35 GPa by DFT+ U calculations, the lattice of stetindite phase is still stable and persists. The calculated phonon spectra by DFPT approach revealed the softening of the E_g^1 rotational mode, and it becomes imaginary between 12 and 16 GPa, indicating lattice instability. Integrating both experimental findings with HPLS phase at ~ 15 GPa and computational analyses from this study, it leads to the conclusion of a second-order phase transition driven by a softening mode. The resultant twist in the oxygen cage breaks the symmetry element, leading to the transition from stetindite ($I4_1/amd$) to lower symmetry. The E_g^1 mode has not been observed experimentally due to its low frequency, highlighting the need for either further low-frequency Raman scattering or single crystal high-pressure X-ray diffraction studies. Overall, this work suggests that the phase transition of CeSiO₄: stetindite \rightarrow scheelite is predominantly lattice dynamically driven by the softening of the E_g^1 mode, offering valuable insights into the behavior of these materials under extreme pressure conditions and laying the foundation for future research on the intermediate high-pressure low-symmetry phase.

Conflicts of interest

There are no conflicts of interest to declare.

Author contributions

Xiaofeng Guo and Liang Qi conceived the idea, provided supervision and draft revision. Xiaodong Zhao performed the calculations, analyzed the data and wrote the initial draft. Andrew C. Strzelecki provided the experimental results and enrolled in the discussion of the results. All the members are enrolled in the manuscript writing and discussion.

Acknowledgements:

We acknowledge the supports by the National Science Foundation (NSF), Division of Earth Sciences, under award No. 2149848, and Division of Materials Research, under award No. 2144792. This research used resources from the Center for Institutional Research Computing at Washington State University. Portions of this research were supported by the WSU-PNNL Nuclear Science and Technology Institute, and Alexandra Navrotsky Institute for Experimental Thermodynamics. Xiaodong Zhao also acknowledges Yihui Wei (University of Utah) for help of acquiring computing resource and the beneficial discussion with Micah Prange (Pacific Northwest National Laboratory).

Reference:

- (1) Guo, X.; Szenknect, S.; Mesbah, A.; Labs, S.; Clavier, N.; Poinssot, C.; Ushakov, S. V.; Curtius, H.; Bosbach, D.; Ewing, R. C.; Burns, P.; Dacheux, N.; Navrotsky A. Thermodynamics of formation of coffinite, USiO₄. *Proceedings of the National Academy of Sciences* **2015**, *112* (21), 6551-6555.
- (2) Ewing, R. C.; Weber, W. J.; Lian, J. Nuclear waste disposal—Pyrochlore (A 2 B 2 O 7): Nuclear waste form for the immobilization of plutonium and “minor” actinides. *Journal of Applied Physics* **2004**, *95* (11), 5949-5971.
- (3) Whipple, C. G. Can nuclear waste be stored safely at yucca mountain? *Scientific American* **1996**, *274* (6), 72-79.
- (4) Ojovan, M. I.; Yuditsev, S. V. Glass, ceramic, and glass-crystalline matrices for HLW immobilisation. *Open Ceramics* **2023**, *14*, 100355.
- (5) Starks, J. *Purex process*; Du Pont de Nemours (EI) and Co., Aiken, SC (USA). Savannah River Plant, 1977.
- (6) Ewing, R.; Lutze, W.; Weber, W. J. Zircon: A host-phase for the disposal of weapons plutonium. *Journal of Materials Research* **1995**, *10*, 243-246.
- (7) Brown, K. L. *Plutopia: Nuclear families, atomic cities, and the great Soviet and American plutonium disasters*; Oxford University Press, USA, 2013.
- (8) Horwitz, E.; Schulz, W. The Truex process: A vital tool for disposal of US defense nuclear waste. *New separation chemistry techniques for radioactive waste and other specific applications* **1991**, 21-29.
- (9) Choppin, G.; Morgenstern, A. Radionuclide separations in radioactive waste disposal. *Journal of Radioanalytical and Nuclear Chemistry* **2000**, *243* (1), 45-51.
- (10) McCloy, J. S.; Goel, A. Glass-ceramics for nuclear-waste immobilization. *MRS bulletin* **2017**, *42* (3),

233-240.

(11) Caurant, D.; Loiseau, P.; Majerus, O.; Aubin-Chevaldonnet, V.; Bardez, I.; Quintas, A. *Glasses, glass-ceramics and ceramics for immobilization of highly radioactive nuclear wastes*; Nova Science Hauppauge, 2007.

(12) Keller, C. *Untersuchungen über die Germanate und Silikate des Typs ABO₄ der vierwertigen Elemente Thorium bis Americium*; Gesellschaft für Kernforschung mbh, 1963.

(13) Speer, J. The actinide orthosilicates. *Reviews in Mineralogy and Geochemistry* **1980**, 5 (1), 113-135.

(14) Ewing, R. C. The design and evaluation of nuclear-waste forms: clues from mineralogy. *The Canadian Mineralogist* **2001**, 39 (3), 697-715.

(15) Ewing, R. C. Nuclear waste forms for actinides. *Proceedings of the National Academy of Sciences* **1999**, 96 (7), 3432-3439.

(16) Weber, W. J.; Ewing, R. C.; Angell, C. A.; Arnold, G. W.; Cormack, A. N.; Delaye, J. M.; Griscom, D. L.; Hobbs, L. W.; Navrotsky, A.; Price, D. L. Radiation effects in glasses used for immobilization of high-level waste and plutonium disposition. *Journal of Materials Research* **1997**, 12 (8), 1948-1978.

(17) Strzelecki, A. C.; Zhao, X.; Estevenon, P.; Xu, H.; Dacheux, N.; Ewing, R. C.; Guo, X. Crystal Chemistry and Thermodynamic Properties of Zircon Structure-Type Materials. *American Mineralogist* **2024**, 109, 225-242.

(18) Migdisov, A.; Nisbet, H.; Li, N.; White, J.; Xu, H.; Nelson, A.; Roback, R. Instability of U₃Si₂ in pressurized water media at elevated temperatures. *Communications Chemistry* **2021**, 4 (1), 65.

(19) Data, E. N. R. National Nuclear Data Center. *Brookhaven National Laboratory* (<http://www.nndc.bnl.gov/exfor/exfor00.htm>) and *International Atomic Energy Agency, Nuclear Data Services* (<http://www-nds.iaea.org/exfor/exfor.htm>) **2000**.

(20) Deditius, A. P.; Utsunomiya, S.; Ewing, R. C. The chemical stability of coffinite, USiO₄·nH₂O; 0 < n < 2, associated with organic matter: A case study from Grants uranium region, New Mexico, USA. *Chemical Geology* **2008**, 251 (1-4), 33-49.

(21) Deditius, A. P.; Utsunomiya, S.; Ewing, R. C. Alteration of Coffinite (USiO₄) Under Reducing and Oxidizing Conditions. *MRS Online Proceedings Library* **2006**, 985, 1-6.

(22) Janeczek, J.; Ewing, R. Coffinitization—a mechanism for the alteration of UO₂ under reducing conditions. *MRS Online Proceedings Library (OPL)* **1991**, 257, 497.

(23) Szenknect, S.; Mesbah, A.; Cordara, T.; Clavier, N.; Brau, H.-P.; Le Goff, X.; Poinssot, C.; Ewing, R. C.; Dacheux, N. First experimental determination of the solubility constant of coffinite. *Geochimica et Cosmochimica Acta* **2016**, 181, 36-53.

(24) Hazen, R. M.; Ewing, R. C.; Sverjensky, D. A. Evolution of uranium and thorium minerals. *American Mineralogist* **2009**, 94 (10), 1293-1311.

(25) Zhang, F.; Pointeau, V.; Shuller, L.; Reaman, D.; Lang, M.; Liu, Z.; Hu, J.; Panero, W.; Becker, U.; Poinssot, C. Structural transitions and electron transfer in coffinite, USiO₄, at high pressure. *American Mineralogist* **2009**, 94 (7), 916-920.

(26) Bauer, J.; Labs, S.; Weiss, S.; Bayarjargal, L.; Morgenroth, W.; Milman, V.; Perlov, A.; Curtius, H.; Bosbach, D.; Zänker, H. High-pressure phase transition of coffinite, USiO₄. *The Journal of Physical Chemistry C* **2014**, 118 (43), 25141-25149.

(27) Strzelecki, A. C.; Barral, T.; Estevenon, P.; Mesbah, A.; Goncharov, V.; Baker, J.; Bai, J.; Clavier, N.; Szenknect, S.; Migdisov, A.; Xu, H.; Ewing, R. C.; Dacheux, N.; Guo, X. The role of water and hydroxyl groups in the structures of stetindite and coffinite, MSiO₄ (M= Ce, U). *Inorganic Chemistry* **2021**, 60 (2), 718-735.

(28) Barral, T.; Estevenon, P.; Chanteau, Y.; Kaczmarek, T.; Strzelecki, A. C.; Menut, D.; Welcomme, E.; Szenknect, S.; Moisy, P.; Guo, X.; Dacheux, N. How hydrothermal synthesis improves the synthesis of (Zr, Ce) SiO₄ solid solutions. *Dalton Transactions* **2023**, 52 (29), 10023-10037.

(29) Ferriss, E.; Ewing, R.; Becker, U. Simulation of thermodynamic mixing properties of actinide-containing zircon solid solutions. *American Mineralogist* **2010**, 95 (2-3), 229-241.

(30) Strzelecki, A. C.; Zhao, X.; Baker, J. L.; Estevenon, P.; Barral, T.; Mesbah, A.; Popov, D.; Chariton, S.; Prakapenka, V.; Ahmed, S.; Yoo, C.; Dacheux, N.; Xu, H.; Guo, X. High-pressure structural and

- thermodynamic properties of cerium orthosilicates (CeSiO₄). *The Journal of Physical Chemistry C* **2023**, *127* (8), 4225-4238.
- (31) Strzelecki, A. C.; Bourgeois, C.; Kriegsman, K. W.; Estevenon, P.; Wei, N.; Szenknect, S.; Mesbah, A.; Wu, D.; Ewing, R. C.; Dacheux, N.; Guo, X. Thermodynamics of CeSiO₄: implications for actinide orthosilicates. *Inorganic Chemistry* **2020**, *59* (18), 13174-13183.
- (32) Estevenon, P.; Welcomme, E.; Tamain, C.; Jouan, G.; Szenknect, S.; Mesbah, A.; Poinssot, C.; Moisy, P.; Dacheux, N. The formation of PuSiO₄ under hydrothermal conditions. *Dalton Transactions* **2020**, *49* (19), 6434-6445.
- (33) Estevenon, P.; Welcomme, E.; Szenknect, S.; Mesbah, A.; Moisy, P.; Poinssot, C.; Dacheux, N. Study of the hydrothermal synthesis of ThSiO₄, USiO₄ and CeSiO₄ aiming at determining the conditions of PuSiO₄ formation. In *2017 E-MRS Fall Meeting*, 2017.
- (34) Xu, H.; Wang, Y. Prediction of thermodynamic property of Pu-zircon and Pu-pyrochlore. In *AIP Conference Proceedings*, 2000; AIP Publishing: Vol. 532, pp 363-363.
- (35) Dacheux, N.; Estevenon, P.; Strzelecki, A. C.; Szenknect, S.; Moisy, P.; Ewing, R.; Guo, X.; Navrotsky, A. Formation of CeSiO₄ and AnSiO₄ (An= Th, U, Pu): insights coming from hydrothermal synthesis and thermodynamic issues. In *Goldschmidt 2023 Conference*, 2023; GOLDSCHMIDT.
- (36) Mihailova, B.; Waesermann, N.; Stangarone, C.; Angel, R. J.; Prencipe, M.; Alvaro, M. The pressure-induced phase transition (s) of ZrSiO₄ ZrSiO₄: revised: Experimental proof for the existence of a new high-pressure polymorph of zircon. *Physics and Chemistry of Minerals* **2019**, *46*, 807-814.
- (37) Kresse, G.; Furthmüller, J. Efficiency of ab-initio total energy calculations for metals and semiconductors using a plane-wave basis set. *Computational Materials Science* **1996**, *6* (1), 15-50. DOI: [https://doi.org/10.1016/0927-0256\(96\)00008-0](https://doi.org/10.1016/0927-0256(96)00008-0).
- (38) Kresse, G.; Furthmüller, J. Software VASP, vienna (1999). *Phys. Rev. B* **1996**, *54* (11), 169.
- (39) Kresse, G.; Hafner, J. Ab initio molecular dynamics for liquid metals. *Physical review B* **1993**, *47* (1), 558.
- (40) Kresse, G. *Comput. matter sci.* *6*, 15 (1996);(d) kresse, g., and furthmuller. *Phys. Rev. B* **1996**, *54*, 11-169.
- (41) Blöchl, P. E. Projector augmented-wave method. *Physical Review B* **1994**, *50* (24), 17953-17979. DOI: 10.1103/PhysRevB.50.17953.
- (42) Kresse, G.; Joubert, D. From ultrasoft pseudopotentials to the projector augmented-wave method. *Physical Review B* **1999**, *59* (3), 1758-1775. DOI: 10.1103/PhysRevB.59.1758.
- (43) Emery, A. A.; Wolverton, C. High-Throughput DFT calculations of formation energy, stability and oxygen vacancy formation energy of ABO₃ perovskites. *Scientific data* **2017**, *4*, 170153.
- (44) Baroni, S.; De Gironcoli, S.; Dal Corso, A.; Giannozzi, P. Phonons and related crystal properties from density-functional perturbation theory. *Reviews of modern Physics* **2001**, *73* (2), 515.
- (45) Togo, A.; Chaput, L.; Tadano, T.; Tanaka, I. Implementation strategies in phonopy and phono3py. *Journal of Physics: Condensed Matter* **2023**.
- (46) Togo, A. First-principles phonon calculations with phonopy and phono3py. *Journal of the Physical Society of Japan* **2023**, *92* (1), 012001.
- (47) Togo, A.; Tanaka, I. First principles phonon calculations in materials science. *Scripta Materialia* **2015**, *108*, 1-5.
- (48) Aroyo, M. I.; Perez-Mato, J. M.; Capillas, C.; Kroumova, E.; Ivantchev, S.; Madariaga, G.; Kirov, A.; Wondratschek, H. Bilbao Crystallographic Server: I. Databases and crystallographic computing programs. *Zeitschrift für Kristallographie-Crystalline Materials* **2006**, *221* (1), 15-27.
- (49) Syme, R.; Lockwood, D.; Kerr, H. Raman spectrum of synthetic zircon (ZrSiO₄) and thorite (ThSiO₄). *Journal of Physics C: Solid State Physics* **1977**, *10* (8), 1335.
- (50) Su, L.; Wan, L.; Gao, T.; Ao, B. First-principles calculations of the electronic structure, chemical bonding, and thermodynamic properties of USiO₄. *AIP Advances* **2020**, *10* (7).
- (51) Li, Z.; John, S. T. Phonon anomaly in high-pressure Zn. *Physical Review Letters* **2000**, *85* (24), 5130.
- (52) Parlinski, K.; Kawazoe, Y. Ab initio study of phonons in the rutile structure of under pressure. *The European Physical Journal B-Condensed Matter and Complex Systems* **2000**, *13* (4), 679-683.

- (53) Albuquerque, A. R.; Maul, J.; Longo, E.; Dos Santos, I. M.; Sambrano, J. R. Hydrostatic and [001] uniaxial pressure on anatase TiO₂ by periodic B3LYP-D* calculations. *The Journal of Physical Chemistry C* **2013**, *117* (14), 7050-7061.
- (54) Kresse, G. VASP the Guide. <http://cms.mpi.univie.ac.at/vasp/> **2001**.
- (55) Tian, L. Density Functional Study of Elastic Properties of Metallic Alloys. KTH Royal Institute of Technology, 2015.
- (56) Doll, K. Analytical stress tensor and pressure calculations with the CRYSTAL code. *Molecular Physics* **2010**, *108* (3-4), 223-227.
- (57) Weber, V.; Tymczak, C. J.; Challacombe, M. Energy gradients with respect to atomic positions and cell parameters for the Kohn-Sham density-functional theory at the Γ point. *The Journal of chemical physics* **2006**, *124* (22).
- (58) Poirier, J.-P.; Tarantola, A. A logarithmic equation of state. *Physics of the Earth and Planetary Interiors* **1998**, *109* (1-2), 1-8.
- (59) Gonzalez-Platas, J.; Alvaro, M.; Nestola, F.; Angel, R. EosFit7-GUI: a new graphical user interface for equation of state calculations, analyses and teaching. *Journal of Applied Crystallography* **2016**, *49* (4), 1377-1382.
- (60) Stangarone, C.; Angel, R. J.; Prencipe, M.; Campomenosi, N.; Mihailova, B.; Alvaro, M. Measurement of strains in zircon inclusions by Raman spectroscopy. *European Journal of Mineralogy* **2019**, *31* (4), 685-694.
- (61) Geisler, T.; Burakov, B. E.; Zirlin, V.; Nikolaeva, L.; PÖML, P. A Raman spectroscopic study of high-uranium zircon from the Chernobyl "lava". *European Journal of Mineralogy* **2005**, *17* (6), 883-894.
- (62) Clavier, N.; Szenknect, S.; Costin, D.; Mesbah, A.; Poinssot, C.; Dacheux, N. From thorite to coffinite: A spectroscopic study of Th_{1-x}U_xSiO₄ solid solutions. *Spectrochimica Acta Part A: Molecular and Biomolecular Spectroscopy* **2014**, *118*, 302-307.